This is a preprint, the final version is subject to change, of the American Mineralogist (MSA)
Cite as Authors (Year) Title. American Mineralogist, in press.
DOI: https://doi.org/10.2138/am-2019-6887

Revision 1: Determination of the oxidation state of iron in Mid-Ocean Ridge basalt glasses by Raman spectroscopy

Charles Le Losq[1], Andrew J. Berry[1], Mark A. Kendrick[1], Daniel R. Neuville[2], Hugh St. C. O'Neill[1]

[1]Research School of Earth Sciences, Australian National University, Canberra, ACT 2601, Australia.

[2]Géomatériaux, Institut de Physique du Globe de Paris, CNRS, Paris University, Paris 75005, France.

Abstract

A series of synthetic Mid-Ocean Ridge Basalt (MORB) glasses with Fe^{3+}/Fe^{TOT} from 0 to 1, determined previously by Mössbauer spectroscopy, was used to test methods for quantifying Fe^{3+}/Fe^{TOT} by Raman spectroscopy. Six numerical data reduction methods were investigated, based on conventional approaches as well as supervised and unsupervised machine learning algorithms. For the set of glass standards, with fixed composition, the precision of all methods was $\leq \pm 0.04$ (one standard deviation). However, Raman spectra recorded for 42 natural MORB glasses from a wide range of locations revealed a strong correlation between the Raman spectra and composition, despite the latter varying only over a relatively limited range, such that the methods calibrated using the glass standards are not directly applicable to the natural samples. This compositional effect can be corrected by using a compositional term that links spectral variations to Fe^{3+}/Fe^{TOT} of the glass. The resulting average Fe^{3+}/Fe^{TOT} determined by Raman spectroscopy was 0.090 ± 0.067 (n=42). This value agrees with the latest Fe K-edge XANES and wet-chemistry estimates of 0.10 ± 0.02. The larger uncertainty of the Raman determination reflects the sensitivity of Raman spectroscopy to small changes in glass structure. While this sensitivity is detrimental for high precision Fe^{3+}/Fe^{TOT} determinations, it allows the major element composition of natural MORB glasses to be determined within 1 mol% through the use of a neural network. This suggests that Raman spectrometers may be used to determine the composition of samples *in situ* at difficult to access locations that are incompatible with X-ray spectrometry (e.g. Mid-Ocean Ridges). Raman spectroscopy may also be useful in detecting changes in the oxidation state of Fe in volcanic glasses where high spatial resolution is required (e.g., melt inclusions), and other compositional variation is not an issue.

Keywords: Mid-ocean ridge basalt, glass, Raman spectroscopy, iron, oxidation state, redox, machine learning

1. Introduction

Mid-Ocean Ridge Basalts (MORB), derived from partial melting of the upper mantle, are central to our understanding of the geochemistry of the mantle and the formation of the oceanic crust (e.g. Langmuir et al. 1992; Asimow et al. 2004; O'Neill and Jenner 2012; Gale et al. 2013) MORB glasses, formed by rapid cooling at the rim of pillow lavas, enable the composition of the melts to be determined (e.g., Jenner and O'Neill 2012), including volatile contents (Kendrick et al. 2013), and oxidation states (Christie et al. 1986; Bézos and Humler 2005; Cottrell and Kelley 2011, 2013; Berry et al. 2018; Zhang et al. 2018; O'Neill et al. 2018). This, in turn, allows the intensive and extensive thermodynamic conditions of the mantle source to be calculated (e.g. Asimow et al. 2004). In particular, the oxidation state of Fe in MORB, expressed as Fe^{3+}/Fe^{TOT} with $Fe^{TOT} = Fe^{2+} + Fe^{3+}$, is important because it affects estimates of temperature, mineral assemblages, and the speciation of volatile elements, both during the production of the parental magmas in the mantle and their subsequent low-pressure evolution.

The latest average Fe^{3+}/Fe^{TOT} values of natural MORB glasses from global sources have been determined to be 0.10 ± 0.02 (Berry et al. 2018) and 0.14 ± 0.01 (Zhang et al. 2018) by Fe K-edge XANES spectroscopy, and 0.11 ± 0.02 by wet-chemistry (corrected for plagioclase phenocrysts, Bézos and Humler 2005). Wet chemistry is a destructive method that lacks spatial resolution and is unsuitable for inhomogeneous glasses or small samples such as melt inclusions (e.g., see Bézos and Humler 2005). Fe K-edge XANES spectroscopy has excellent precision and micron spatial resolution in two dimensions, but requires glass standards that are compositionally matched and for which Fe^{3+}/Fe^{TOT} has been determined by another technique, such as ^{57}Fe Mössbauer spectroscopy (e.g. Berry et al. 2008). There are also questions concerning possible photo-oxidation during analysis of hydrous glasses (e.g. Cottrell et al. 2018). A considerable drawback for routine analysis is that it requires access to a synchrotron light source.

Raman spectroscopy is an alternative technique for determining Fe^{3+}/Fe^{TOT} that is often readily accessible without delay, is non-destructive, has micron-scale spatial resolution, requires minimal sample preparation, is easy to perform, and spectra can be acquired within minutes. Previous studies have shown how Raman spectroscopy can be used for quantifying the concentration of H_2O (Thomas 2000; Zajacz et al. 2005; Behrens et al. 2006; Thomas et al. 2008; Mercier et al. 2009, 2010; Le Losq et al. 2012) and CO_2 (Amalberti et al. 2012; Morizet et al. 2013) in glasses, with applications to pumices and melt inclusions (Shea et al. 2014; Métrich et al. 2016). The potential of Raman spectroscopy to determine Fe^{3+}/Fe^{TOT} in glasses has been demonstrated previously using various data treatment protocols (Magnien et al., 2004, 2006, 2008; Roskosz et al., 2008; Di Muro et al., 2009; Di Genova et al., 2016). The simplest method requires correlating changes in Fe^{3+}/Fe^{TOT} with changes in the intensity of the Raman spectra at a given Raman shift (Magnien et al. 2006; Roskosz et al. 2008). A more complex method involves peak fitting the Raman signals assigned to stretching of tetrahedral SiO_4 and AlO_4 units in order to extract the Fe^{3+}-O signal, which can be related to Fe^{3+}/Fe^{TOT} (Di Muro et al. 2009; Welsch et al. 2017). Recently, Di Genova et al. (2016) proposed another approach based on interpolation between two endmember spectra (*e.g.*, oxidized and reduced glasses of the same composition). These different studies focused on demonstrating the ability of Raman spectroscopy to quantify Fe^{3+}/Fe^{TOT} in glasses of known composition.

Methods for quantifying Fe^{3+}/Fe^{TOT} of glasses from Raman spectra have relied on either simple treatments (e.g. the intensity of one or more peaks, mixing end-member spectra) or peak fitting. To our knowledge, machine learning algorithms, which remove subjectivity in the data reduction protocol, have not yet been tested. Here we compare existing data reduction methods (*conventional methods*), based on spectral intensity variations and mixing of spectra, with new supervised and unsupervised machine learning approaches. We avoided the peak fitting procedure (e.g. Di Muro et al. 2009) because it is complex to perform and equivocal of interpretation (Welsch et al. 2017), and thus may not be suited to a routine protocol. Conventional methods and supervised machine learning require the Fe^{3+}/Fe^{TOT} values of the glass standards to be known. Unsupervised machine learning methods, however, do not require prior knowledge of Fe^{3+}/Fe^{TOT} of the standards, such that they offer an independent way of determining Fe^{3+}/Fe^{TOT} for comparison with the results of other techniques. Those methods were assessed for a set of 13 synthetic glasses with a typical but simplified MORB composition and known Fe^{3+}/Fe^{TOT} (Berry et al. 2018). Following the proof of concept, the methods were used to determine Fe^{3+}/Fe^{TOT} of a representative set of 42 natural MORB glasses from the Atlantic, Indian and Pacific oceans, with known major and trace elements compositions

(Melson et al. 2002; Jenner and O'Neill 2012; Kendrick et al. 2013) and Fe K-edge XANES Fe^{3+}/Fe^{TOT} values (Berry et al. 2018).

2. Material and Methods

2.1 Starting Glasses

The MORB standards were prepared from mixtures of reagent grade SiO_2 (52.0 wt%), Al_2O_3 (16.1 wt%), $CaCO_3$ = CaO (12.4 wt%), Fe_2O_3 = FeO (10.0 wt%), MgO (8.2 wt%) and TiO_2 (1.3 wt%) that were equilibrated at 1400 ˚C and values of log fO_2 between 0 and -11 (-4.7 and 6.3 in log units relative to the quartz-fayalite-magnetite, QFM, buffer) for ~ 24 h before quenching in water. A sample was also prepared at logfO_2 = 4.8 (QFM + 11.2) using a piston-cylinder apparatus. The Fe^{3+}/Fe^{TOT} ratio of each glass was determined by Mössbauer spectroscopy, and found to vary from ~ 0 to 1 (Table 1). For further details see Berry et al. (2018).

Samples of natural MORB glass were obtained from the Department of Mineral Sciences, Smithsonian Institution, as polished chips mounted in epoxy resin and are listed by MNNH catalogue numbers in Supplementary Table 1. The sample details and major element composition are given in Melson et al. (2002), their trace element composition in Jenner and O'Neill (2012), and their Fe^{3+}/Fe^{TOT} values determined by Fe K-edge XANES spectroscopy in Berry et al. (2018). From the set analysed by Berry et al. (2018), the Raman spectra of five glasses (NMNH No. 111235-85, 115083-41, 113828-5, 111241-1, 111237-67) were contaminated by contributions from crystals (see supplementary code) and were not considered during the data reduction. Five samples studied previously by Kendrick et al. (2013) from Juan de Fuca (Alv 2262-8 and Alv 2269-2), the East Pacific Rise Clipperton (CL DR01) and Mid-Atlantic Ridge MAPCO (CH98 DR08 and CH98 DR11) were also analysed as polished sections in epoxy resin.

2.2 Raman Spectra Acquisition

Raman spectra of glasses were recorded using a Renishaw inVia™ spectrometer, equipped with a Peltier-cooled detector, a 2400 l/mm grating and a confocal system. Samples were excited using a 532 nm laser line focused ~ 3 μm below the surface using a x100 Leica objective. The laser power on the sample was ~ 1.2 mW. The spatial resolution was < 1 μm, and the spectral resolution ~ 1.2 cm^{-1}. Five spectra were recorded from different points for each sample. They were treated separately during the data reduction process. The acquisition time varied between 120 and 180 s. For water-bearing natural MORB samples, oxidation of Fe by the laser has been reported at high laser power (Di Genova et al. 2017). The combination of a laser power less than 5 mW (Di Genova et al. 2017) with a relatively short counting time of 120 s, and the analysis at five different spots, was used to prevent Fe oxidation during spectral acquisition. We checked this by recording Raman maps for six samples, by acquiring 120 spectra with an acquisition time of 1 s over an area of 10 μm by 12 μm. During the acquisition of these maps, the sample was continuously moved, such that the beam spent less than 1 s at a given location. The individual spectra were noisy, but their average produced a spectrum with a signal to noise ratio similar to that of a spectrum acquired in 120 s at a single point. No difference was observed between spectra obtained in these two ways, indicating that no variation of Fe^{3+}/Fe^{TOT} was induced during the acquisition.

To investigate differences in spectrometer, laser wavelength, and signal-to-noise ratio (S/N), as would be expected between laboratories, spectra were also acquired using a T64000 Jobin-Yvon® Raman triple spectrometer equipped with a confocal system, a nitrogen-cooled 1024 CCD detector, and a 488 nm Coherent® 70-C5 Ar^+ laser operating at 1.8 W. A 1/100 filter was inserted in the laser pathway to ensure that laser power on the sample was less than 2 mW and a 100x Olympus® objective was used for analysis. This setup allows a spatial resolution < 1 μm, and a spectral resolution of ~ 0.7 cm^{-1}. Acquisition time was tuned to deteriorate the S/N such that, with this setup, the average S/N in the 800-1300 cm^{-1} portion of the spectra was ~20, compared to over 60 for the inVia™ Renishaw system.

2.3 Data pre-processing

The spectra (Fig. 1) were pre-processed in Python using the Rampy library (Le Losq, 2018). The data were corrected for temperature and excitation line effects following Galeener and Sen (1978). We focused the data reduction methods on the 800-1300 cm^{-1} region of the spectra, which contains signals from Si-O, Al-O and Fe^{3+}-O stretching in the glass structure (Brawer and White 1975, 1977; Virgo et al. 1980; Mysen et al. 1982; Virgo et al. 1982). This region also avoided signals due to nanolites (< 800 cm^{-1}), which were observed in the spectra of some of the natural glasses (see supplementary materials). We chose to fit a linear baseline to subtract the background (Fig. 2A), with the aim of having only Si-O, Al-O and Fe^{3+}-O stretching signals in the background-corrected spectra that will be used for Fe^{3+}/Fe^{TOT} determination. The low and high frequency anchors of the linear baseline were determined using a grid-search algorithm as those resulting in the lowest root mean square error (RMSE) between the Mössbauer Fe^{3+}/Fe^{TOT} values and those predicted by the *intensity* and *mixing* methods described in sections 2.4.1 and 2.4.2. This resulted in the subtraction of a linear baseline interpolated between the intensities at 850 and 1140 cm^{-1} (Fig. 2A). The baseline corrected spectra were smoothed using a Whittaker function to maximize the signal to noise ratio (Eilers 2003; see supplementary code for an example), and then the intensity normalised to vary between 0 and 1 (Fig 2B). The spectra resulting from this arbitrary baseline correction cannot be used to infer the glass structure. However, the correction provides a simple method for isolating variations in the Raman signals related to changes in Fe oxidation state (Fig 2B). Furthermore, the arbitrary baseline correction was found to be beneficial because it avoids the introduction of random errors associated with variations in the real spectral background when the sample signal is low (e.g. near 1250 cm^{-1}).

2.4 Determining the oxidation state of iron by Raman spectroscopy

In this study, six different methods were evaluated for determining the oxidation state of Fe in the suite of MORB glass standards (Table 1) from the background subtracted 850-1140 cm^{-1} region of the Raman spectra (Fig. 2B). The idea is to relate, for a set of glass standards with fixed major element composition, changes in the Raman spectra to changes in Fe^{3+}/Fe^{TOT}. The six methods investigated are described below.

2.4.1 Intensity method

The intensity of the Raman spectra between 850 and 1140 cm^{-1} varies systematically with Fe^{3+}/Fe^{TOT} in the glass standards (Figs. 1, 2B). In particular, the intensity at 930 cm^{-1} varies strongly with Fe^{3+}/Fe^{TOT}. This feature has contributions from Fe^{3+}-O (Virgo et al. 1982; Magnien et al. 2006; Di Muro et al. 2009), and thus should be ideal for determining Fe^{3+}/Fe^{TOT}. Two methods were tested to quantify the intensity at 930 cm^{-1}: direct measurement at fixed frequency (the average of values between 929 and 931 cm^{-1}) and peak fitting the 850-1140 cm^{-}

This is a preprint, the final version is subject to change, of the American Mineralogist (MSA)
Cite as Authors (Year) Title. American Mineralogist, in press.
DOI: https://doi.org/10.2138/am-2019-6887

^{1} spectral envelop with arbitrary Gaussian components. Direct measurements of the intensity at 930 cm^{-1} (hereafter abbreviated I_{930}) provided the better precision and this approach was used.

2.4.2 Mixing method

The *Mixing* method is based on the bilinear model that describes the matrix dataset $D_{n,m}$, of dimension *n* spectra times *m* features (i.e. Raman shifts), as:

$$D_{n,m} = F_{n,k} \cdot S_{k,m} + \varepsilon_{n,m} \, , \qquad (1)$$

where $F_{n,k}$ is the matrix of component fractions, $S_{k,m}$ the matrix of partial spectral components (endmember spectra), *k* the number of components and $\varepsilon_{n,m}$ a noise term. In the present case, $k = 2$ (reduced and oxidised endmembers), as verified by a principal component analysis of the 13 standards, which revealed that two components account for more than 99.8% of the variance in the data. Using the notation S_{OX} and S_{RED} to designate the oxidised ($Fe^{3+}/Fe^{TOT} = 1$) and reduced ($Fe^{3+}/Fe^{TOT} = 0$) Raman spectral components, and F_{OX} as the fraction of S_{OX}, eq. (1) can be re-arrange as:

$$D_{n,m} = F_{\mathrm{OX}} \cdot S_{\mathrm{OX}} + (1 - F_{\mathrm{OX}}) \cdot S_{\mathrm{RED}} \, . \qquad (2)$$

We used least absolute regression (LAD) to determine F_{OX}, because LAD is more robust than least squares with respect to outliers or non-Gaussian distributions (Tarantola 2005). The optimised F_{OX} values can then be related to the glass Fe^{3+}/Fe^{TOT} values (Di Genova et al., 2016).

2.4.3 Alternative Least Square Multivariate Curve Resolution (ALS MCR)

Solving eq. (1) usually requires either $F_{n,k}$ or $S_{k,m}$. For example, $F_{n,k}$ are obtained from $S_{k,m}$ in the *Mixing* method (sec. 2.4.2). However, several techniques allow both $F_{n,k}$ and $S_{k,m}$ to be estimated from $D_{n,m}$, including independent component analysis (e.g. Hyvärinen et al. 2001), non-negative matrix factorisation (e.g. Lin 2007), iterative optimisation (e.g. Zakaznova-Herzog et al. 2007), and self-modelling curve resolution (Jiang et al. 2004; de Juan and Tauler

Always consult and cite the final, published document. See http:/www.minsocam.org or GeoscienceWorld

2006), also known as multivariate curve resolution. As they do not require prior knowledge of neither $F_{n,k}$ nor $S_{k,m}$ (see eq. 1), those methods belong to the class of unsupervised machine learning algorithms. For the present dataset of spectra, several conditions need to be satisfied: (i) $F_{n,k} \in [0,1]$; (ii) $F_{n,1} = 1 - F_{n,2}$; and (iii) $S_{k,m} \in \mathbb{R}^{+}$. Of the available methods, multivariate curve resolution can help solve the present problem with respecting those conditions.

In this study, the *ALS MCR* method was used to iteratively optimise $F_{n,k}$ and $S_{k,m}$. The PyMCR python library was used, starting the algorithm with estimations of $S_{k,m}$ obtained from mean spectra in our spectral dataset. The algorithm was allowed to perform 50 iterations. After convergence, usually achieved in only a few iterations, optimised $F_{n,k}$ and $S_{k,m}$ matrices are available for the investigated dataset. The spectral endmembers stored in the optimised $S_{k,m}$ matrix (i.e. optimised F_{OX} and F_{RED}) can then be used with the *Mixing* method for new samples.

Convergence of the *ALS MCR* algorithm is inherently dependent on the starting conditions (e.g. Valderrama et al. 2016). The effects of the range of $\mathrm{Fe^{3+}/Fe^{TOT}}$ values included in $D_{n,m}$, and the starting $S_{k,m}$ components, were tested using iterative protocols. The $\mathrm{Fe^{3+}/Fe^{TOT}}$ dataset range can be represented by two variables: (i) Δ $\mathrm{Fe^{3+}/Fe^{TOT}}$ of $D_{n,m}$, which represents the difference in $\mathrm{Fe^{3+}/Fe^{TOT}}$ between the most reduced and the most oxidized samples in the dataset; and (ii) mean $\mathrm{Fe^{3+}/Fe^{TOT}}$ of $D_{n,m}$, which is the mean value of $\mathrm{Fe^{3+}/Fe^{TOT}}$ for the dataset. Similarly, variations in the initial $S_{k,m}$ components are represented using two parameters: (i) Δ $\mathrm{Fe^{3+}/Fe^{TOT}}$ of $S_{k,m}$ represents the difference in $\mathrm{Fe^{3+}/Fe^{TOT}}$ between the two initial $S_{k,m}$ components; and (ii) mean $\mathrm{Fe^{3+}/Fe^{TOT}}$ of $S_{k,m}$, which is the average $\mathrm{Fe^{3+}/Fe^{TOT}}$ of the two initial $S_{k,m}$ components.

To determine how the root-mean-square deviations between the estimated and nominal $\mathrm{Fe^{3+}/Fe^{TOT}}$ values of the standard vary with Δ $\mathrm{Fe^{3+}/Fe^{TOT}}$ and mean $\mathrm{Fe^{3+}/Fe^{TOT}}$ of $D_{n,m}$, and Δ $\mathrm{Fe^{3+}/Fe^{TOT}}$ and mean $\mathrm{Fe^{3+}/Fe^{TOT}}$ of $S_{k,m}$, these values were varied by iteration, such that different subsets of $D_{n,m}$ and $S_{k,m}$ were generated. These subsets were provided to the *ALS MCR* algorithm to calculate optimised $S_{k,m}$ and $D_{n,m}$ matrices. These optimised matrices were then used to determine $\mathrm{Fe^{3+}/Fe^{TOT}}$ for the entire $D_{n,m}$ and $S_{k,m}$ datasets.

2.4.4 Neural Networks, Kernel Ridge and Support Vector regressions

The three other techniques that were investigated used the supervised machine learning regression algorithms *Neural Networks*, *Kernel Ridge,* and *Support Vector* from the Scikit Learn library (Pedregosa et al. 2011). An interface for using these algorithms with Raman data was implemented in the Rampy library (Le Losq 2018) through the class *mlregressor* (see the Jupyter notebook in the supplementary materials as well as the *rampy.mlregressor* help). The machine learning algorithms require the data to be divided into two subsets: a *training subset* to train the different algorithms, and a *testing subset* that are treated as unknowns to evaluate the predictive error of the algorithms. The train-test split was performed by randomly sorting the dataset according to their Fe^{3+}/Fe^{TOT} values (function *chemical_splitting* from the rampy library). The testing data subset was ~ 38 % of the total dataset.

The *Neural Network* technique uses a network of activation units, which are Rectifier functions [$y = max(0,x)$] (Glorot et al. 2011) in the present study, to map the relationship between the Raman spectra and Fe^{3+}/Fe^{TOT} values of the glasses (see description in Bengio 2009 and references therein). The activation units have adjustable parameters, called weights and biases, that are optimised by least square regression. This method makes no assumptions about the linearity of variations in the Raman spectra with Fe^{3+}/Fe^{TOT}. The network was optimised by testing different architectures to minimize the training and testing errors, and to keep those two values as close as possible to each other. A simple architecture with three activation units in a single hidden layer provided the most robust fits. Adding more activations units or layers did not decrease the error metrics of the network, and hence this simple architecture was used. The Limited-memory Broyden-Fletcher-Goldfarb-Shanno (*lbfgs*) solver was chosen, as it performs better than others for the present small dataset. Bagging, which consists of training multiple networks and returning the average of their outputs (Breiman and Breiman 1996), was performed to avoid over-fitting and to promote the ability of the network to predict new values. A total of 100 networks were trained, and the results represent the average output of these 100 networks.

The *Kernel Ridge* and *Support Vector* techniques regress the data after their projection in a high-dimensionality space. This projection was done using a non-linear radial basis kernel function, such that the Raman intensity can non-linearly depend on Fe^{3+}/Fe^{TOT}. The difference between the *Kernel Ridge* and *Support Vector* regressions lies in the use of different loss functions: *Kernel Ridge* regression uses a penalized (l_2 normalisation) residual of the sum of squares, whereas *Support Vector* regression uses a ε-insensitive loss function (ε is a deviation term in the loss function, i.e. the predictions are allowed to be as far from the calibration data as ε). More information on these algorithms is available in Murphy (2012), Smola and Schölkopf (2004) and Vapnik (1999). The hyper-parameters of the *Kernel Ridge* and *Support Vector* algorithms were automatically tuned by performing a random 5-fold cross-validation on the training dataset.

A Jupyter notebook running under the Python language, together with all the spectra, are provided as supplementary materials to enable the results of this study, and the figures, to be reproduced.

3. Results

3.1 Raman spectra of MORB glass standards

The Raman spectra of the MORB glass standards exhibit peaks and shoulders at ~ 505, 570, 660, 735, 804, 930 and 1005 cm^{-1} (A to G markers in Fig. 1), with intensities that depend on Fe^{3+}/Fe^{TOT}. The intensities of the A, B, C and D Raman signals decrease with decreasing Fe^{3+}/Fe^{TOT} (Fig. 1, Table 1), whereas those of E and G increase (Figs. 1, 2B). The intensity of F relative to that of G decreases with decreasing Fe^{3+}/Fe^{TOT} (Fig. 2B).

The changes in the Raman spectra of the glasses following changes in Fe^{3+}/Fe^{TOT} reflect changes in (i) the Fe^{3+} contribution to the Raman signals, and (ii) the overall glass structure as Fe^{3+} and Fe^{2+} have different roles. The signals in the 810-1300 cm^{-1} region of the Raman spectra of MORB glasses can be assigned to symmetric and asymmetric stretching of Q^n SiO_4-AlO_4 units, where n is the number of bridging oxygens (Brawer and White 1975, 1977; Furukawa and White 1980; Furukawa et al. 1981; Mysen et al. 1982; McMillan 1984; Mysen 1990; Neuville and Mysen 1996; Neuville et al. 2004; Neuville 2006; Neuville et al. 2008; Le Losq and Neuville 2013; Le Losq et al. 2014). The intensity at F is assigned to the combination of signals from Fe^{3+}-O stretching in the glass network (Virgo et al. 1982; Wang et al. 1995; Magnien et al. 2004, 2006, 2008; Di Muro et al. 2009; Cochain et al. 2012) and Si-O stretching in Q^2 units (Virgo et al. 1980; Mysen et al. 1982; McMillan 1984). This assignment agrees with (i) the decrease in the relative intensity of F with reduction of Fe (Figs. 1, 2B) and (ii) the presence of F as a shoulder in the spectra of the most reduced samples (Figs. 1, 2B). The peak near 1005 cm^{-1} mainly comprises contributions from Si-O and Al-O stretching in Q^3 units. This signal usually occurs near 1100 cm^{-1} in Al-free silicate glasses (e.g. Mysen et al. 1982; McMillan 1984) but shifts to lower frequencies in aluminosilicate glasses (Neuville and Mysen 1996; Mysen et al. 2003; Le Losq and Neuville 2013). This assignment is consistent with the composition of MORB glasses; with NBO/T values ranging from ~ 0.5 to ~ 1.0 (see Chapter 17 in Mysen and Richet 2005), they are expected to be enriched in Q^3 units and to contain minor fractions of Q^2 and Q^4 (e.g. Maekawa et al. 1991).

3.2 Raman spectroscopy as a tool for determining Fe^{3+}/Fe^{TOT} of MORB glasses

3.2.1 The Intensity method

I_{930} in the Raman spectra of the synthetic MORB glasses is linearly correlated with Fe^{3+}/Fe^{TOT} (Fig. 3), with a correlation coefficient of 0.9973. It is thus possible to determine Fe^{3+}/Fe^{TOT} of a glass from the I_{930} scaled Raman intensity using the equation:

$$Fe^{3+}/Fe^{TOT} = 4.084(38) \times I_{930} - 2.779(29)\ . \tag{3}$$

The root-mean-square deviation between the Fe^{3+}/Fe^{TOT} values of the standards and those calculated with eq. 3 is 0.02 (1σ).

3.2.2 The Mixing method

Following a protocol similar to that described by Di Genova et al. (2016), we used the spectra of the most oxidized and reduced glasses (log fO_2 = 4.8 and -11.0, Table 1) as endmembers. Then, F_{OX} was adjusted by least absolute regression to obtain mixed spectra that matched the observed ones (Fig. 4A). F_{OX} is linearly proportional to Fe^{3+}/Fe^{TOT} (Fig. 4B) with a correlation coefficient of 0.9974. This result differs from the finding of Di Genova et al. (2016), who reported non-linear variations of F_{OX} with Fe^{3+}/Fe^{TOT} for rhyolitic and basaltic glasses. This may be due to the fact that these authors did not use endmember spectra with Fe^{3+}/Fe^{TOT} = 0 and 1, but of intermediate values. In the present case, F_{OX} and Fe^{3+}/Fe^{TOT} are related by:

$$Fe^{3+}/Fe^{TOT} = 1.02(1) \times F_{OX} - 0.003(4)\ . \qquad (4)$$

F_{OX} directly gives Fe^{3+}/Fe^{TOT} of MORB glasses to within 0.03 (1σ).

3.2.3 The ALS MCR method

For a set of glasses with unknown but varying Fe^{3+}/Fe^{TOT} values, *ALS MCR* can determine the endmember spectra (i.e. spectra corresponding to $Fe^{3+}/Fe^{TOT} = 0$ and 1), and hence, Fe^{3+}/Fe^{TOT} for any MORB glass by linear combination fitting.

Figure 5 presents the results obtained from tests performed to evaluate the sensitivity of *ALS MCR* to the starting conditions (see sec. 2.4.3). The best results were obtained when the dataset covered the largest possible range of Fe^{3+}/Fe^{TOT} values, i.e. when Δ Fe^{3+}/Fe^{TOT} of $D_{n,m} \rightarrow 1$ and mean Fe^{3+}/Fe^{TOT} of $D_{n,m} \rightarrow \sim 0.4 - 0.5$ (Fig. 5A). Fe^{3+}/Fe^{TOT} root-mean-square deviations < 0.06 were achieved using datasets with Δ Fe^{3+}/Fe^{TOT} of $D \geq 0.75$ and mean Fe^{3+}/Fe^{TOT} of D $\in [0.35,0.55]$. The choice of the initial $S_{k,m}$ affects the accuracy of the *ALS MCR* method in a less extent than the choice of the initial $D_{n,m}$ (Fig. 5B). Fe^{3+}/Fe^{TOT} root-mean-square deviations < 0.03 were obtained for initial $S_{k,m}$ with mean $Fe^{3+}/Fe^{TOT} \in [0.4,0.6]$ and Δ $Fe^{3+}/Fe^{TOT} \in [0.1,0.6]$.

The *ALS MCR* method was tested further by optimising $S_{k,m}$ using the full dataset $D_{n,m}$. From Figure 5B, initial S components with Δ Fe^{3+}/Fe^{TOT} and mean Fe^{3+}/Fe^{TOT} of ~ 0.5 and 0.4, respectively, should provide the best results. Thus, the mean spectra at $Fe^{3+}/Fe^{TOT} = 0.66$ and 0.25 were selected as initial $S_{k,m}$ components. Selecting mean spectra with $Fe^{3+}/Fe^{TOT} = 0$ and 1 does not significantly change the results, but the present choice allows the effects of differences in the initial and optimised $S_{k,m}$ components to be illustrated, as shown in Figure 6A. The optimised $S_{k,m}$ spectra are clearly different from their initial values, demonstrating the ability of *ALS MCR* to identify the true $S_{k,m}$ endmembers. The optimised $S_{k,m}$ produce good fits to the observed spectra (Fig. 6B). The fraction of the oxidised endmember, C_{OX}, is linearly related to the Fe^{3+}/Fe^{TOT} of the glass by (Fig. 6C):

$$Fe^{3+}/Fe^{TOT} = 1.07(1) \times C_{OX} - 0.035(5)\ . \qquad (5)$$

Contrary to F_{OX}, C_{OX} is not directly equal to $\mathrm{Fe}^{3+}/\mathrm{Fe}^{\mathrm{TOT}}$. This is because of small differences between the optimised $S_{k,m}$ endmembers and the mean Raman spectra at $\mathrm{Fe}^{3+}/\mathrm{Fe}^{\mathrm{TOT}} = 0$ and 1 (residuals shown in Fig. 6A). These differences introduce a bias, such that using C_{OX} as a direct estimate of $\mathrm{Fe}^{3+}/\mathrm{Fe}^{\mathrm{TOT}}$ leads to slightly (~ 0.02) under- and over-estimations of $\mathrm{Fe}^{3+}/\mathrm{Fe}^{\mathrm{TOT}}$, depending on the $\mathrm{Fe}^{3+}/\mathrm{Fe}^{\mathrm{TOT}}$ value. Because of this, the root-mean-square deviation between the Raman-determined and standard $\mathrm{Fe}^{3+}/\mathrm{Fe}^{\mathrm{TOT}}$ values is ± 0.04 when assuming $F_{\mathrm{OX}} = C_{\mathrm{OX}}$. Slightly better results were obtained using eq. 5, which allows $\mathrm{Fe}^{3+}/\mathrm{Fe}^{\mathrm{TOT}}$ of the glasses to be determined within ± 0.03 (Table 1).

3.2.4 Neural Networks, Kernel Ridge and Support Vector regression methods

The *Neural Network*, *Kernel Ridge*, and *Support Vector* methods performed very well with both the training and testing datasets (Fig. 7), with root-mean-square deviations between the measured and predicted $\mathrm{Fe}^{3+}/\mathrm{Fe}^{\mathrm{TOT}}$ values of ~ 0.01-0.03 (Table 1). For all methods, the root-mean-square deviations for the training dataset were slightly lower than that for the testing dataset, indicating that the machine-learning algorithms tended to slightly over-fit the training dataset. Over-fitting is not desirable because it indicates that the *generalisation* ability of the algorithms (i.e. their ability to predict values for new samples) may not be optimal. However, in the present case, the difference between the training and testing standard deviations is small (≤ 0.02), and the over-fitting is considered to be negligible. Therefore, these algorithms can be used to predict $\mathrm{Fe}^{3+}/\mathrm{Fe}^{\mathrm{TOT}}$ of MORB glasses with an error $\leq \pm 0.03$ (1σ).

3.2.5 Is there a better method?

The root-mean-square deviations between the $\mathrm{Fe}^{3+}/\mathrm{Fe}^{\mathrm{TOT}}$ values determined by Mössbauer and Raman spectroscopy are < 0.04 for all six methods. The *Intensity* and *Mixing* methods are as accurate and precise as those using machine learning (*ALS MCR, Neural Network*, *Kernel Ridge* and *Support Vector*; Table 1).

The choice of method depends on the aims of the study and the dataset. If a single data reduction method was to be chosen, the simplicity of the *Intensity* and *Mixing* methods makes these appealing. If $\mathrm{Fe}^{3+}/\mathrm{Fe}^{\mathrm{TOT}}$ of the standards are unknown, the *ALS MCR* method may allow

$S_{k,m}$ components to be extracted and Fe^{3+}/Fe^{TOT} to be determined, if the dataset covers a large range of Fe^{3+}/Fe^{TOT} values (Fig. 5). The *Intensity*, *Mixing* and *ALS MCR* methods all rely on linear variations between Raman signals and Fe^{3+}/Fe^{TOT} of the glasses. In contrast, the *Neural Network*, *Kernel Ridge*, and *Support Vector* methods do not assume linearity and do not require the mathematical form of the variations to be known.

Ultimately, we recommend the use of multiple data reduction methods, as undertaken here, to test the consistency of results. This is desirable because each data reduction protocol may be differently sensitive to how differences in composition affect the Raman spectra (Fig. 2B). Therefore, following a Bayesian approach, the average of the results from all the methods should be more robust than any single estimate (e.g. Perrone 1993). In the present case, such an approach is easy to implement because all the methods presented in this study are simple to setup and cheap in terms of computing resources. Averaging the results of the six models to determine Fe^{3+}/Fe^{TOT} of the glasses from their Raman spectra resulted in a root-mean-square deviation of 0.02 (1σ).

3.2.6 Application to natural MORB glasses

The baseline subtracted and normalised Raman spectra of natural MORB glasses are shown in Figure 8A (see supplementary Jupyter Notebook for full spectra). While the spectra are similar to that of the glass standard with $Fe^{3+}/Fe^{TOT} = 0.106$, non-negligible differences are apparent (Fig. 8A). I_{930} varies between 0.66 and 0.76, and is correlated with the concentration of MgO and CaO in the glass (Pearson correlation coefficient = 0.73`, Fig. 8B). For the glass standards, a difference of ~ 0.10 in I_{930} corresponds to a difference in Fe^{3+}/Fe^{TOT} of ~ 0.40 (Fig. 3). For these spectra, the six methods described give an average Fe^{3+}/Fe^{TOT} of 0.15 with a large standard deviation of 0.11.

It is possible to refine this estimate by including a compositional term in the expressions relating Raman features to Fe^{3+}/Fe^{TOT}. We focused on the *Intensity method* and expressed I_{930} as:

$$I_{930} = (K0 + K1 \times Fe^{3+}/Fe^{TOT}) + K2 \times X \,, \qquad (6)$$

where X is a parameter reflecting the chemistry of the samples, and K0, K1 and K2 constants. X could be chosen as either [MgO+CaO] or the number of non-bridging oxygens per tetrahedral unit (NBO/T) in the glass. Increasing [MgO + CaO] favours the formation of non-bridging oxygens and thus of depolymerised Q^2 units in basaltic glasses, which give signals near 950 cm^{-1} (e.g. Mysen et al. 1982). This is consistent with the positive trend observed between I_{930} and [MgO + CaO] (Fig. 8B). However, while NBO/T parameterises the general effect of differences in the fraction of network formers (e.g. Si, Al) and network modifiers (e.g. Na, K, Ca, Mg) on the glass structure, it does not consider the effect of the ionic properties of network modifiers on the distribution of Q^n units, which contribute to the Raman intensity between 850 and 1140 cm^{-1}. For example, at a constant NBO/T of 0.5 for alkali silicate glasses, the fractions of Q^4 and Q^2 increase at the expense of Q^3 as the ionic field strength (Z/r^2, where Z is the electric charge and r the ionic radius) of the alkali metal cation increases (Maekawa et al. 1991). The ionic field strength of metal cations also influences other structural properties of silicate glasses and melts, including the fraction of highly-coordinated Al, excess NBO, and Si-Al disorder (see Le Losq et al. 2019 for a review). As a result, to describe changes in the Raman spectra due to variations in the sample composition, we used the mean ionic field strength (IFS) of network modifiers (M), IFS(M), as the X parameter in eq. (6):

$$IFS(M) = 2x_{Na_2O} \times IFS(Na^+) + 2x_{K_2O} \times IFS(K^+) + x_{CaO} \times IFS(Ca^{2+}) + x_{MgO} \times IFS(Mg^{2+}) + x_{FeO} \times IFS(Fe^{2+}) \text{ ,} \quad (7)$$

where $x_{M^{z+}_{2/z}O}$ are the mol fractions of the oxide components $M^{z+}_{2/z}O$, and IFS of a cation M^{z+} is calculated as Z/r^2. The r values were taken from Shannon (1976) for coordination numbers (CN) of 6. For simplicity, we do not consider variations in CN since these are likely to be negligible given the limited range of compositional variability in MORB. We also consider FeO as equal to total Fe because Fe^{3+}/Fe^{TOT} of natural MORB is always low (~0.1) and constant (e.g. Berry et al. 2018; Zhang et al. 2018), such that any influence of Fe on the glass structure will come from variations in x_{FeO}.

The correlation between I_{930} and IFS(M) is linear for natural MORB glasses (Fig. 9). The ordinate at the origin of this trend corresponds to K0 + K1× Fe^{3+}/Fe^{TOT}, and its slope to K2. K1 is directly given by the linear trend between Fe^{3+}/Fe^{TOT} and I_{930} (Fig. 3), and is equal to 0.2435(23), while K2 equals 0.00624(29). It then is trivial to determine K0 as 0.111(27). Using these parameters, it is possible to plot iso-redox curves of IFS(M) versus I_{930}, as shown in Fig. 9. A visual inspection indicates that the natural samples have a mean Fe^{3+}/Fe^{TOT} value ~ 0.1, although there is significant scatter. Manipulating eq. (7) to extract Fe^{3+}/Fe^{TOT} values for natural MORB from K0, K1, K2 and I_{930} yields a mean Fe^{3+}/Fe^{TOT} of 0.090(67).

3.2.7 Effect of acquisition conditions

Applying the methods calibrated using the spectra acquired with the Renishaw system to the spectra acquired with the T64000 Jobin-Yvon® system (see section 2.2 for details about acquisition conditions and supplementary Jupyter notebook for data visualization) resulted in the standard deviation between the Mössbauer and Raman Fe^{3+}/Fe^{TOT} values increasing from 0.02 to 0.08. Part of this increase in uncertainty can be assigned to the decrease in spectral S/N (from > 60 to ~ 20). However, Fe^{3+}/Fe^{TOT} values > 0.5 appear to be under-estimated and have the largest effect on the average error. This may indicate that the Raman cross-sections of the Si-O and Fe^{3+}-O stretching modes change at different rates when varying the laser wavelength. The results may also be affected by different frequency responses of the different CCD detectors.

Based on those observations, it is important to record spectra with high S/N (> 60) to be able to have accurate predictions of Fe^{3+}/Fe^{TOT}. Decreasing the S/N will lead to a progressive deterioration in the precision of the predicted Fe^{3+}/Fe^{TOT} values. If different spectrometers and laser wavelengths are used, the accuracy of any previously calibrated algorithms should be checked using standards.

4. Discussion

Both conventional methods (*Intensity*, *Mixing*) and machine learning algorithms (*ALS MCR, Kernel Ridge, Support Vector* and *Neural Network*) allow Fe^{3+}/Fe^{TOT} to be determined from the Raman spectra of glasses, with fixed major element composition, with uncertainties < 0.04 (Table 1). The combination of all six methods gives a precision of 0.02. The *Intensity* and *Mixing* methods are simple and provide accurate results. The machine learning methods performed well despite being trained with a limited set of samples. The *ALS MCR* method may be useful if the Fe^{3+}/Fe^{TOT} values of the glass standards are unknown, or if endmember spectra are not available. *Kernel Ridge, Support Vector* and *Neural Network* regression algorithms relate Fe^{3+}/Fe^{TOT} of the glasses to variations in their Raman spectra without any assumptions about the form of the variations. Pooling the results from multiple data reduction protocols is recommended for maximizing the robustness of Fe^{3+}/Fe^{TOT} determinations for glasses with a fixed composition.

The determination of Fe^{3+}/Fe^{TOT} in natural MORB glasses requires a correction for the effect of composition on the Raman spectra (Figs. 8B, 9, eq. 7). The corrected mean value of $Fe^{3+}/Fe^{TOT} = 0.090(67)$ is in agreement with the latest XANES and wet chemistry results (Bézos and Humler 2005; Berry et al. 2018; Zhang et al. 2018). In particular, this estimate is in close agreement with the XANES value of 0.10(1) reported by Berry et al. (2018) for the same set of samples, which suggests an average fO_2 for MORB of 0.1 log units above the QFM redox buffer.

Raman spectroscopy can thus provide reasonable estimates of Fe^{3+}/Fe^{TOT} in glasses, as long as the effect of glass chemistry is considered. High precision can be achieved for laboratory samples with constant chemical composition. However, the present results do not achieve the precision of Fe K-edge XANES, Mössbauer spectroscopy or wet chemistry for natural samples with variable chemical composition without the introduction of a compositional term. Compositional effects originating from variations in major element concentrations were corrected using eq. (6), but other factors that affect glass structure (and hence the Raman spectra), such as volatile content and quench rate, were not considered. The high standard deviation affecting the Fe^{3+}/Fe^{TOT} estimate most probably reflects the occurrence of such effects. Further, while eq. (6) is valid for MORB glasses, it may not be suitable for determining Fe^{3+}/Fe^{TOT} in other compositions. However, with a set of appropriate standards, Raman spectroscopy could be used to quantify Fe^{3+}/Fe^{TOT} in any composition. In all cases, the routine determination of Fe^{3+}/Fe^{TOT} in natural samples by Raman spectroscopy will be challenging due to the many variables that affect glass structure.

5. Implications

Machine learning techniques do not seem to be advantageous relative to conventional approaches for quantifying Fe^{3+}/Fe^{TOT} in glasses with constant composition by Raman spectroscopy. However, their ease of implementation and flexibility (the problem can be non-linear) make them preferable to other user-defined techniques when the functional form of the problem is unknown. In particular, the sensitivity of Raman spectra to glass structure can be used to determine glass composition. Di Genova et al. (2015; 2016) used the mixing method to determine the composition of natural glasses from Raman spectra. This required a post-analysis step in the data treatment as the mixing ratio of end-member spectra varied non-linearly with glass composition. In the present case, we trained a neural network to directly link the corrected 850-1140 cm^{-1} Raman signals (Fig. 8A) to the measured concentrations of major elements in the natural MORB glasses (supplementary materials), without any additional data manipulation. The results from one of the trained neural networks are shown in Figure 10. The network was able to predict the chemistry of MORB glasses with errors $< \sim 1$ mol%. This result suggests that Raman spectroscopy may be developed as a chemical probe. It also demonstrates the usefulness of neural networks for such calculations, as the algorithm directly provides the glass composition without intermediate data analysis steps. The approach could allow Raman spectroscopy to be used *in situ* to analyse pillow lavas with glassy rims at ocean ridges, by using submersibles equipped with Raman spectrometers already developed for deep sea water analysis (e.g. Brewer et al. 2004; White et al. 2005; Du et al. 2015). Raman spectrometers could also be used as a chemical probe in missions to planets or moons with dense atmospheres. The fact that all data processing performed in this study uses Python, a programming language that can be easily used in embedded systems would facilitate uptake. The present approach should be easy to implement for any system operating a portable Raman spectrometer.

Acknowledgement

The Department of Mineral Sciences, Smithsonian Institution, is thanked for providing the samples of MORB glass. H.O.N thanks the Australian Research Council for the award of a Laureate Fellowship (FL130100066). C.L.L. thanks Guil Mallmann for helpful discussions. The authors thank an anonymous reviewer for helpful comments.

References

Amalberti, J., Neuville, D.R., Sarda, P., Sator, N., and Guillot, B. (2012) Quantification of CO_2 dissolved in silicate glasses and melts using Raman spectroscopy: implications for geodynamics. Mineralogical Magazine, 76.

Asimow, P.D., Dixon, J.E., and Langmuir, C.H. (2004) A hydrous melting and fractionation model for mid-ocean ridge basalts: Application to the Mid-Atlantic Ridge near the Azores. Geochemistry, Geophysics, Geosystems, 5.

Behrens, H., Roux, J., Neuville, D., and Siemann, M. (2006) Quantification of dissolved H_2O in silicate glasses using confocal microRaman spectroscopy. Chemical Geology, 229, 96–112.

Bengio, Y. (2009) Learning Deep Architectures for AI. Foundations and Trends® in Machine Learning, 2, 1–127.

Berry, A.J., Danyushevsky, L.V., O'Neill, H.S.C., Newville, M., and Sutton, S.R. (2008) Oxidation state of iron in komatiitic melt inclusions indicates hot Archaean mantle. Nature, 455, 960–963.

Berry, A.J., Stewart, G.A., O'Neill, H.S.C., Mallmann, G., and Mosselmans, J.F.W. (2018) A re-assessment of the oxidation state of iron in MORB glasses. Earth and Planetary Science Letters, 483, 114–123.

Bézos, A., and Humler, E. (2005) The $Fe^{3+}/\Sigma Fe$ ratios of MORB glasses and their implications for mantle melting. Geochimica et Cosmochimica Acta, 69, 711–725.

Brawer, S.A., and White, W.B. (1975) Raman spectroscopic investigation of the structure of silicate glasses. I. The binary alkali silicates. The Journal of Chemical Physics, 63, 2421–2432.

——— (1977) Raman spectroscopic investigation of the structure of silicate glasses (II). Soda-alkaline earth-alumina ternary and quaternary glasses. Journal of Non-Crystalline Solids, 23, 261–278.

Breiman, L., and Breiman, L. (1996) Bagging Predictors. In Machine Learning pp. 123–140.

Brewer, P.G., Malby, G., Pasteris, J.D., White, S.N., Peltzer, E.T., Wopenka, B., Freeman, J., and Brown, M.O. (2004) Development of a laser Raman spectrometer for deep-ocean science. Deep Sea Research Part I: Oceanographic Research Papers, 51, 739–753.

Christie, D.M., Carmichael, I.S.E., and Langmuir, C.H. (1986) Oxidation states of mid-ocean ridge basalt glasses. Earth and Planetary Science Letters, 79, 397–411.

Cochain, B., Neuville, D.R., Henderson, G.S., McCammon, C.A., Pinet, O., and Richet, P. (2012) Effects of the iron content and redox state on the structure of sodium borosilicate glasses: A Raman, Mössbauer and boron K-Edge XANES spectroscopy study. Journal of the American Ceramic Society, 95, 962–971.

Cottrell, E., and Kelley, K.A. (2011) The oxidation state of Fe in MORB glasses and the oxygen fugacity of the upper mantle. Earth and Planetary Science Letters, 305, 270–282.

——— (2013) Redox heterogeneity in mid-ocean ridge basalts as a function of mantle source. Science, 340, 1314–1317.

Cottrell, E., Lanzirotti, A., Mysen, B.O., Birner, S., Kelley, K.A., Botcharnikov, R.E., Davis, F.A., and Newville, M. (2018) A Mössbauer-based XANES calibration for hydrous basalt glasses reveals radiation-induced oxidation of Fe. American Mineralogist, 103, 489–501.

de Juan, A., and Tauler, R. (2006) Multivariate Curve Resolution (MCR) from 2000: Progress in Concepts and Applications. Critical Reviews in Analytical Chemistry, 36, 163–176.

Di Genova, D., Morgavi, D., Hess, K.-U., Neuville, D.R., Borovkov, N., Perugini, D., and Dingwell, D.B. (2015) Approximate chemical analysis of volcanic glasses using Raman spectroscopy. Journal of Raman Spectroscopy, 46, 1235–1244.

Di Genova, D., Hess, K.-U., Chevrel, M.O., and Dingwell, D.B. (2016) Models for the estimation of Fe^{3+}/Fe^{tot} ratio in terrestrial and extraterrestrial alkali- and iron-rich silicate glasses using Raman spectroscopy. American Mineralogist, 101, 943–952.

Di Genova, Danilo, Kolzenburg, S., Vona, A., Chevrel, M.O., Hess, K.-U., Neuville, D.R., Ertel-Ingrisch, W., Romano, C., and Dingwell, D.B. (2016) Raman spectra of Martian glass analogues: A tool to approximate their chemical composition. Journal of Geophysical Research: Planets, 121, 2016JE005010.

Di Genova, D., Sicola, S., Romano, C., Vona, A., Fanara, S., and Spina, L. (2017) Effect of iron and nanolites on Raman spectra of volcanic glasses: A reassessment of existing strategies to estimate the water content. Chemical Geology, 475, 76–86.

Di Muro, A., Métrich, N., Mercier, M., Giordano, D., Massare, D., and Montagnac, G. (2009) Micro-Raman determination of iron redox state in dry natural glasses: Application to peralkaline rhyolites and basalts. Chemical Geology, 259, 78–88.

Du, Z., Li, Y., Chen, J., Guo, J., and Zheng, R. (2015) Feasibility investigation on deep ocean compact autonomous Raman spectrometer developed for in-situ detection of acid radical ions. Chinese Journal of Oceanology and Limnology, 33, 545–550.

Eilers, P.H.C. (2003) A perfect smoother. Analytical Chemistry, 75, 3631–3636.

Furukawa, T., and White, W.B. (1980) Vibrational spectra and glass structure. Journal of Non-Crystalline Solids, 38, 87–92.

Furukawa, T., Fox, K.E., and White, W.B. (1981) Raman spectroscopic investigation of the structure of silicate glasses. III. Raman intensities and structural units in sodium silicate glasses. The Journal of Chemical Physics, 75, 3226–3237.

Gale, A., Dalton, C.A., Langmuir, C.H., Su, Y., and Schilling, J.-G. (2013) The mean composition of ocean ridge basalts. Geochemistry, Geophysics, Geosystems, 14, 489–518.

Galeener, F.L., and Sen, P.N. (1978) Theory of the first-order vibrational spectra of disordered solids. Physical Review B, 17, 1928–1933.

Glorot, X., Bordes, A., and Bengio, Y. (2011) Deep sparse rectifier neural networks. In International Conference on Artificial Intelligence and Statistics pp. 315–323.

Hyvärinen, A., Karhunen, J., and Oja, E. (2001) Independent component analysis. John Wiley & Sons, Inc.

Jenner, F.E., and O'Neill, H.S.C. (2012) Analysis of 60 elements in 616 ocean floor basaltic glasses: TECHNICAL BRIEF. Geochemistry, Geophysics, Geosystems, 13, Q02005.

Jiang, J.-H., Liang, Y., and Ozaki, Y. (2004) Principles and methodologies in self-modeling curve resolution. Chemometrics and Intelligent Laboratory Systems, 71, 1–12.

Kendrick, M.A., Arculus, R., Burnard, P., and Honda, M. (2013) Quantifying brine assimilation by submarine magmas: Examples from the Galápagos Spreading Centre and Lau Basin. Geochimica et Cosmochimica Acta, 123, 150–165.

Langmuir, C.H., Klein, E.M., and Plank, T. (1992) Petrological Systematics of Mid-Ocean Ridge Basalts: Constraints on Melt Generation Beneath Ocean Ridges. In Mantle Flow and Melt Generation at Mid-Ocean Ridges pp. 183–280. American Geophysical Union (AGU).

Le Losq, C. (2018) Rampy: a Python library for processing spectroscopic (IR, Raman, XAS...) data. Zenodo.

Le Losq, C., and Neuville, D.R. (2013) Effect of the Na/K mixing on the structure and the rheology of tectosilicate silica-rich melts. Chemical Geology, 346, 57–71.

Le Losq, C., Neuville, D.R., Moretti, R., and Roux, J. (2012) Determination of water content in silicate glasses using Raman spectrometry: Implications for the study of explosive volcanism. American Mineralogist, 97, 779–790.

Le Losq, C., Neuville, D.R., Florian, P., Henderson, G.S., and Massiot, D. (2014) The role of Al^{3+} on rheology and structural changes of sodium silicate and aluminosilicate glasses and melts. Geochimica et Cosmochimica Acta, 126, 495–517.

Le Losq, C., Cicconi, M.R., Greaves, G.N., and Neuville, D.R. (2019) Silicate Glasses. In Handbook of Glass. Springer.

Lin, C.-J. (2007) Projected Gradient Methods for Nonnegative Matrix Factorization. Neural Computation, 19, 2756–2779.

Maekawa, H., Maekawa, T., Kawamura, K., and Yokokawa, T. (1991) The structural groups of alkali silicate glasses determined from ^{29}Si MAS-NMR. Journal of Non-Crystalline Solids, 127, 53–64.

Magnien, V., Neuville, D.R., Cormier, L., Mysen, B.O., Briois, V., Belin, S., Pinet, O., and Richet, P. (2004) Kinetics of iron oxidation in silicate melts: a preliminary XANES study. Chemical Geology, 213, 253–263.

Magnien, V., Neuville, D.R., Cormier, L., Roux, J., Hazemann, J.L., Pinet, O., and Richet, P. (2006) Kinetics of iron redox reactions in silicate liquids: A high-temperature X-ray absorption and Raman spectroscopy study. Journal of Nuclear Materials, 352, 190–195.

Magnien, V., Neuville, D., Cormier, L., Roux, J., Hazemann, J., Deligny, D., Pascarelli, S., Vickridge, I., Pinet, O., and Richet, P. (2008) Kinetics and mechanisms of iron redox reactions in silicate melts: The effects of temperature and alkali cations. Geochimica et Cosmochimica Acta, 72, 2157–2168.

McMillan, P.F. (1984) Structural studies of silicate glasses and melts - Applications and limitations of Raman spectroscopy. American Mineralogist, 69, 622–644.

Melson, W.G., O'Hearn, T., and Jarosewich, E. (2002) A data brief on the Smithsonian Abyssal Volcanic Glass Data File. Geochemistry, Geophysics, Geosystems, 3, 1–11.

Mercier, M., Di Muro, A., Giordano, D., Métrich, N., Lesne, P., Pichavant, M., Scaillet, B., Clocchiatti, R., and Montagnac, G. (2009) Influence of glass polymerisation and oxidation on micro-Raman water analysis in alumino-silicate glasses. Geochimica et Cosmochimica Acta, 73, 197–217.

Mercier, M., Muro, A.D., Métrich, N., Giordano, D., Belhadj, O., and Mandeville, C.W. (2010) Spectroscopic analysis (FTIR, Raman) of water in mafic and intermediate glasses and glass inclusions. Geochimica et Cosmochimica Acta, 74, 5641–5656.

Métrich, N., Bertagnini, A., Garaebiti, E., Vergniolle, S., Bani, P., Beaumais, A., and Neuville, D.R. (2016) Magma transfer and degassing budget: Application to the 2009–2010 eruptive crisis of Mt Garet (Vanuatu arc). Journal of Volcanology and Geothermal Research, 322, 48–62.

Morizet, Y., Brooker, R.A., Iacono-Marziano, G., and Kjarsgaard, B.A. (2013) Quantification of dissolved CO_2 in silicate glasses using micro-Raman spectroscopy. American Mineralogist, 98, 1788–1802.

Murphy, K.P. (2012) Machine Learning: A Probabilistic Perspective. The MIT Press, Cambridge, Massachusetts.

Mysen, B.O. (1990) Role of Al in depolymerized, peralkaline aluminosilicate melts in the systems Li_2O-Al_2O_3-SiO_2, Na_2O-Al_2O_3-SiO_2, and K_2O-Al_2O_3-SiO_2. American Mineralogist, 75, 120–134.

Mysen, B.O., and Richet, P. (2005) Silicate glasses and melts - Properties and structure Vol. 10. Elsevier B.V., Amsterdam.

Mysen, B.O., Finger, L.W., Virgo, D., and Seifert, F.A. (1982) Curve-fitting of Raman spectra of silicate glasses. American Mineralogist, 67, 686–695.

Mysen, B.O., Lucier, A., and Cody, G.D. (2003) The structural behavior of Al^{3+} in peralkaline melts and glasses in the system Na_2O-Al_2O_3-SiO_2. American Mineralogist, 88, 1668–1678.

Neuville, D.R. (2006) Viscosity, structure and mixing in (Ca, Na) silicate melts. Chemical Geology, 229, 28–41.

Neuville, D.R., and Mysen, B.O. (1996) Role of aluminium in the silicate network: In situ, high-temperature study of glasses and melts on the join SiO_2-$NaAlO_2$. Geochimica et Cosmochimica Acta, 60, 1727–1737.

This is a preprint, the final version is subject to change, of the American Mineralogist (MSA)
Cite as Authors (Year) Title. American Mineralogist, in press.
DOI: https://doi.org/10.2138/am-2019-6887

Neuville, D.R., Cormier, L., and Massiot, D. (2004) Al environment in tectosilicate and peraluminous glasses: A ^{27}Al MQ-MAS NMR, Raman, and XANES investigation. Geochimica et Cosmochimica Acta, 68, 5071–5079.

Neuville, D.R., Cormier, L., Montouillout, V., Florian, P., Millot, F., Rifflet, J.-C., and Massiot, D. (2008) Structure of Mg- and Mg/Ca aluminosilicate glasses: ^{27}Al NMR and Raman spectroscopy investigations. American Mineralogist, 93, 1721–1731.

O'Neill, H.S.C., and Jenner, F.E. (2012) The global pattern of trace-element distributions in ocean floor basalts. Nature, 491, 698–704.

O'Neill, H.S.C., Berry, A.J., and Mallmann, G. (2018) The oxidation state of iron in Mid-Ocean Ridge basaltic (MORB) glasses: implications for their petrogenesis and oxygen fugacities. Earth and Planetary Science Letters, 504, 152–162.

Pedregosa, F., Varoquaux, G., Gramfort, A., Michel, V., Thirion, B., Grisel, O., Blondel, M., Prettenhofer, P., Weiss, R., Dubourg, V., and others (2011) Scikit-learn: machine learning in python. Journal of Machine Learning Research, 12, 2825–2830.

Perrone, M.P. (1993) Improving regression estimation: Averaging methods for variance reduction with extensions to general convex measure optimization. Brown University Providence, RI.

Roskosz, M., Toplis, M.J., Neuville, D.R., and Mysen, B.O. (2008) Quantification of the kinetics of iron oxidation in silicate melts using Raman spectroscopy and assessment of the role of oxygen diffusion. American Mineralogist, 93, 1749–1759.

Shannon, R.D. (1976) Revised effective ionic radii and systematic studies of interatomic distances in halides and chalcogenides. Acta Crystallographica Section A: Crystal Physics, Diffraction, Theoretical and General Crystallography, 32, 751–767.

Shea, T., Hellebrand, E., Gurioli, L., and Tuffen, H. (2014) Conduit- to Localized-scale Degassing during Plinian Eruptions: Insights from Major Element and Volatile (Cl and H_2O) Analyses within Vesuvius AD 79 Pumice. Journal of Petrology, 55, 315–344.

Smola, A. J., and Schölkopf, B. (2004) A tutorial on support vector regression. Statistics and Computing, 14, 199–222.

Tarantola, A. (2005) Inverse problem theory and methods for model parameter estimation, 342 p. Society for Industrial and Applied Mathematics, Philadelphia, PA.

Thomas, R. (2000) Determination of water contents of granite melt inclusions by confocal laser Raman microprobe spectroscopy. American Mineralogist, 85, 868–872.

Thomas, R., Metrich, N., Scaillet, B., Kamenetsky, V.S., and Davidson, P. (2008) Determination of water in Fe-rich basalt glasses with confocal micro-Raman spectroscopy. Zeitschrift für Geologische Wissenschaften, 36, 31–37.

Valderrama, L., Gonçalves, R.P., Março, P.H., Rutledge, D.N., and Valderrama, P. (2016) Independent components analysis as a means to have initial estimates for multivariate curve resolution-alternating least squares. Journal of Advanced Research, 7, 795–802.

Always consult and cite the final, published document. See http:/www.minsocam.org or GeoscienceWorld

Vapnik, V., V. (1999) The Nature of Statistical Learning Theory, Second Edition., 332 p. Springer-Verlag, New York.

Virgo, D., Mysen, B.O., and Kushiro, I. (1980) Anionic constitution of 1-Atmosphere silicate melts: implications for the structure of igneous melts. Science, 208, 1371–1373.

Virgo, D., Mysen, B. O., Danckwerth, P., and Seifert, F. (1982) Speciation of Fe^{3+} in 1-atm Na_2O-SiO_2-Fe-O Melts. Carnegie Institution of Washington Year Book, 81, 349–353.

Wang, Z., Cooney, T.F., and Sharma, S.K. (1995) In situ structural investigation of iron-containing silicate liquids and glasses. Geochimica et Cosmochimica Acta, 59, 1571–1577.

Welsch, A.-M., Knipping, J.L., and Behrens, H. (2017) Fe-oxidation state in alkali-trisilicate glasses - A Raman spectroscopic study. Journal of Non-Crystalline Solids, 471, 28–38.

White, S.N., Kirkwood, W., Sherman, A., Brown, M., Henthorn, R., Salamy, K., Walz, P., Peltzer, E.T., and Brewer, P.G. (2005) Development and deployment of a precision underwater positioning system for in situ laser Raman spectroscopy in the deep ocean. Deep Sea Research Part I: Oceanographic Research Papers, 52, 2376–2389.

Zajacz, Z., Halter, W., Malfait, W.J., Bachmann, O., Bodnar, R.J., Hirschmann, M.M., Mandeville, C.W., Morizet, Y., Müntener, O., Ulmer, P., and others (2005) A composition-independent quantitative determination of the water content in silicate glasses and silicate melt inclusions by confocal Raman spectroscopy. Contributions to Mineralogy and Petrology, 150, 631–642.

Zakaznova-Herzog, V.P., Malfait, W.J., Herzog, F., and Halter, W.E. (2007) Quantitative Raman spectroscopy: Principles and application to potassium silicate glasses. Journal of Non-Crystalline Solids, 353, 4015–4028.

Zhang, H.L., Cottrell, E., Solheid, P.A., Kelley, K.A., and Hirschmann, M.M. (2018) Determination of $Fe^{3+}/\Sigma Fe$ of XANES basaltic glass standards by Mössbauer spectroscopy and its application to the oxidation state of iron in MORB. Chemical Geology, 479, 166–175.

Table 1: Synthesis oxygen fugacity at 1400 ˚C, and relative to the quartz-fayalite-magnetite (QFM) buffer, of MORB glass standards (Berry et al. 2018), together with the Fe^{3+}/Fe^{TOT} values determined by Mössbauer spectroscopy (± 0.01), and by Raman spectroscopy using the Intensity (Int.), Mixing (Mix.), ALS MCR (A.M.), Neural Networks (N.N.), Kernel Ridge (K.R.) and Support Vector (S.V.) techniques. Root-mean-squared deviations (RMSD, 1σ) of the different Raman methods are indicated at the bottom; *calculated for the training data subset; $^{\phi}$ calculated for the testing data subset.

log fO_2	**ΔQFM**	**Fe^{3+}/Fe^{TOT}**						
		Mössbauer	**Int.**	**Mix.**	**A.M.**	**N.N.**	**K.R.**	**S.V.**
4.8	11.2	1.000	1.01	0.99	1.01	0.97	1.00	0.97
0.00	6.38	0.773	0.75	0.73	0.75	0.77	0.77	0.75
-1.00	5.40	0.661	0.66	0.63	0.65	0.66	0.66	0.66
-2.00	4.40	0.537	0.53	0.51	0.53	0.54	0.54	0.54
-3.07	3.32	0.414	0.43	0.42	0.43	0.43	0.42	0.44
-4.00	2.39	0.250	0.26	0.25	0.27	0.23	0.27	0.28
-5.00	1.39	0.167	0.16	0.15	0.16	0.14	0.16	0.17
-6.00	0.39	0.103	0.11	0.10	0.11	0.09	0.10	0.10
-7.00	-0.61	0.039	0.01	0.01	0.01	0.05	0.04	0.05
-8.00	-1.61	0.024	0.04	0.04	0.05	0.04	0.03	0.02
-9.00	-2.61	0.017	0.02	0.00	0.01	0.03	0.02	0.01
-10.00	-3.61	0.000	0.00	0.00	-0.01	0.02	0.01	-0.01
-11.00	-4.61	0.000	0.01	0.03	0.01	0.01	0.00	0.01
		RMSD:	0.02	0.03	0.03	0.01* 0.04^{ϕ}	0.01* 0.02^{ϕ}	0.02* 0.03^{ϕ}

This is a preprint, the final version is subject to change, of the American Mineralogist (MSA)
Cite as Authors (Year) Title. American Mineralogist, in press.
DOI: https://doi.org/10.2138/am-2019-6887

Figure 1: Raman spectra of synthetic MORB basaltic glasses; the colors indicate Fe^{3+}/Fe^{TOT}. Each spectrum corresponds to the mean of five spectra acquired for each sample. The dashed lines labelled A-G mark the position of peaks and shoulders (see text).

Figure 2: A) Example of the treatment of the 800-1300 cm^{-1} sections of the Raman spectra that was performed prior to any calculation. The linear cut-off baseline (red dotted line) joins the sample signals at 850 and 1140 cm^{-1}. Any intensity below this baseline was removed from the data. B) Intensity from 850-1140 cm^{-1} after baseline subtraction. This background subtracted region of the spectra was normalised between 0 and 1.

Figure 3: Normalised intensity at 930 cm^{-1} in the Raman spectra of the glasses as a function of the oxidation state of Fe. The line is a linear fit to the data. If not visible, errors are smaller than the symbols.

Figure 4: A) Comparison of the mean spectrum at Fe^{3+}/Fe^{TOT} = 0.41 (black line) and the fit (dotted red line) as a linear combination of the oxidised (S_{OX}) and reduced (S_{RED}) spectra (*Mixing* method); residuals between the data and fit are shown in the bottom panel. B) Fraction of the oxidised endmember spectrum, F_{OX}, as a function of the oxidation state of Fe in the glasses. The line is a linear fit to the data. If not visible, errors are smaller than the symbols.

Figure 5: Contour plots of the root-mean-square deviations (RMSD) between the measured Fe^{3+}/Fe^{TOT} values and those predicted using the *ALS MCR* algorithm using (A) variable training subsets $D_{n,m}$ and (B) different initial $S_{k,m}$ spectra. In (A), RMSD Fe^{3+}/Fe^{TOT} are represented against the mean and the range of Fe^{3+}/Fe^{TOT} values in the data subsets used to train the algorithm. In (B), they are represented against the mean and the range of Fe^{3+}/Fe^{TOT} between the two initial S spectra used to initiate the training. After training, RMSD Fe^{3+}/Fe^{TOT} were estimated on the entire dataset. Black points show where calculations were made; lines and colors were obtained by triangular interpolation.

Figure 6: Results of the *ALS MCR* algorithm using the entire $D_{n,m}$ dataset, with initial (init.) $S_{k,m}$ spectra at Fe^{3+}/Fe^{TOT} = 0.66 and 0.25. A) Initial (init.) and optimised (opt.) oxidised (S_{OX}) and reduced (S_{RED}) endmember spectra; residuals between the optimised S_{OX} and S_{RED} components and the means of spectra recorded for samples with Fe^{3+}/Fe^{TOT} = 0 and 1 are shown in the bottom panel. B) Comparison of the mean spectrum at Fe^{3+}/Fe^{TOT} = 0.41 (black line) and

Always consult and cite the final, published document. See http:/www.minsocam.org or GeoscienceWorld

its fit (dotted red line) obtained by mixing the S_{OX} and S_{RED} endmembers; residual shown in the bottom panel. C) The fraction of the oxidised end-member, C_{OX}, against the Fe^{3+}/Fe^{TOT} values determined by Mössbauer spectroscopy for the MORB glass standards. The line is a linear fit to the data. If not visible, errors are smaller than the symbols.

Figure 7: Raman Fe^{3+}/Fe^{TOT} against Mössbauer Fe^{3+}/Fe^{TOT} values for the MORB glass standards. Raman values were obtained from the A) *Kernel Ridge*, B) *Support Vector*, and C) *Neural Network* algorithms. See Table 1 for root-mean-square deviations of each dataset. If not visible, errors are smaller than the symbols.

Figure 8: A) Normalised baseline-subtracted Raman spectra of 42 natural MORB glasses (see Supplementary Materials). The red dotted line is the spectrum of the glass standard with Fe^{3+}/Fe^{TOT} = 0.10(1). B) I_{930} as a function of the concentration of MgO + CaO (wt%) in the glasses.

Figure 9: I_{930} as a function of the mean ionic field strength of modifier cations, IFS(M) for natural MORB glasses (open symbols) and MORB standards (solid symbols). Dotted lines represent the values of the model (eq. 6, see text) that links I_{930} to IFS(M) and Fe^{3+}/Fe^{TOT} in MORB glasses. The colors reflect the Fe^{3+}/Fe^{TOT} ratio (see colorbar).

Figure 10: Neural network predicted versus measured compositions of natural MORB glasses. The standard deviations between the measured and predicted values for each subset are given for each compositional component.

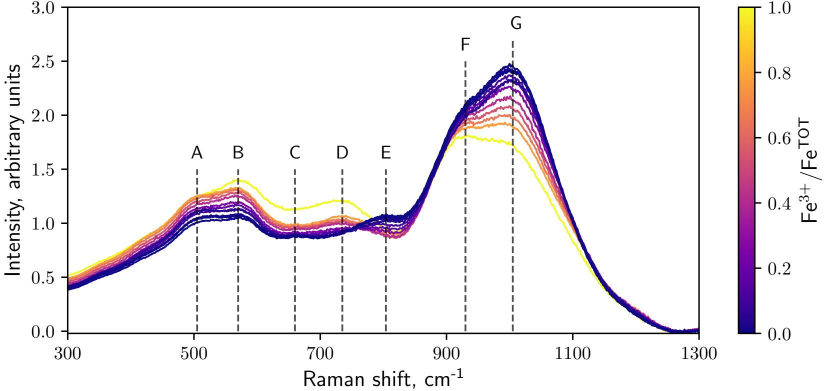
3.0
2.5
2.0
1.5
1.0
0.5
0.0
Intensity, arbitrary units
300
500
700
900
1100
1300
Raman shift, cm^{-1}
A
B
C
D
E
F
G
1.0
0.8
0.6
0.4
0.2
0.0
Fe^{3+}/Fe^{TOT}

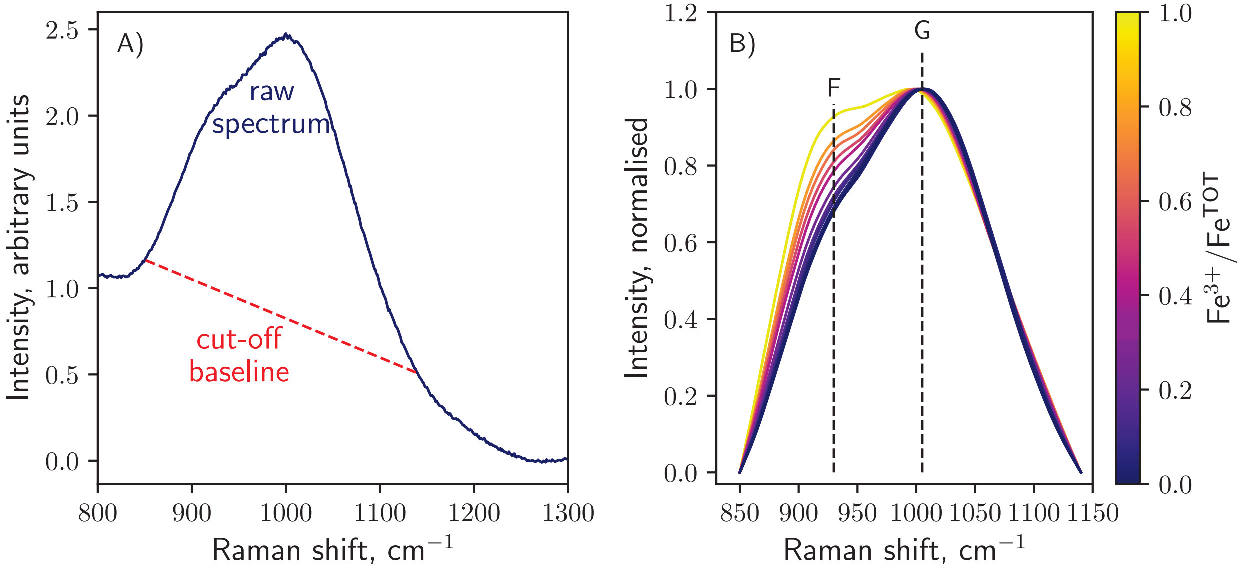
A)
raw spectrum
cut-off baseline
Intensity, arbitrary units
0.0
0.5
1.0
1.5
2.0
2.5
800
900
1000
1100
1200
1300
Raman shift, cm^{-1}
B)
F
G
Intensity, normalised
0.0
0.2
0.4
0.6
0.8
1.0
1.2
850
900
950
1000
1050
1100
1150
Raman shift, cm^{-1}
Fe^{3+}/Fe^{TOT}
0.0
0.2
0.4
0.6
0.8
1.0

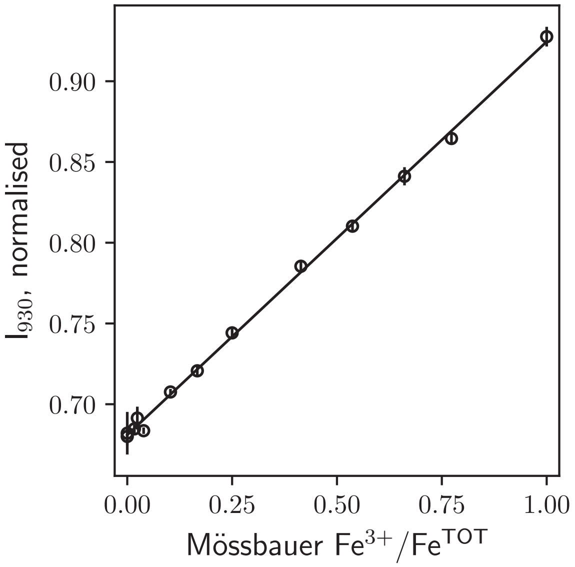
0.70
0.75
0.80
0.85
0.90
0.00
0.25
0.50
0.75
1.00
I_{930}, normalised
Mössbauer Fe^{3+}/Fe^{TOT}

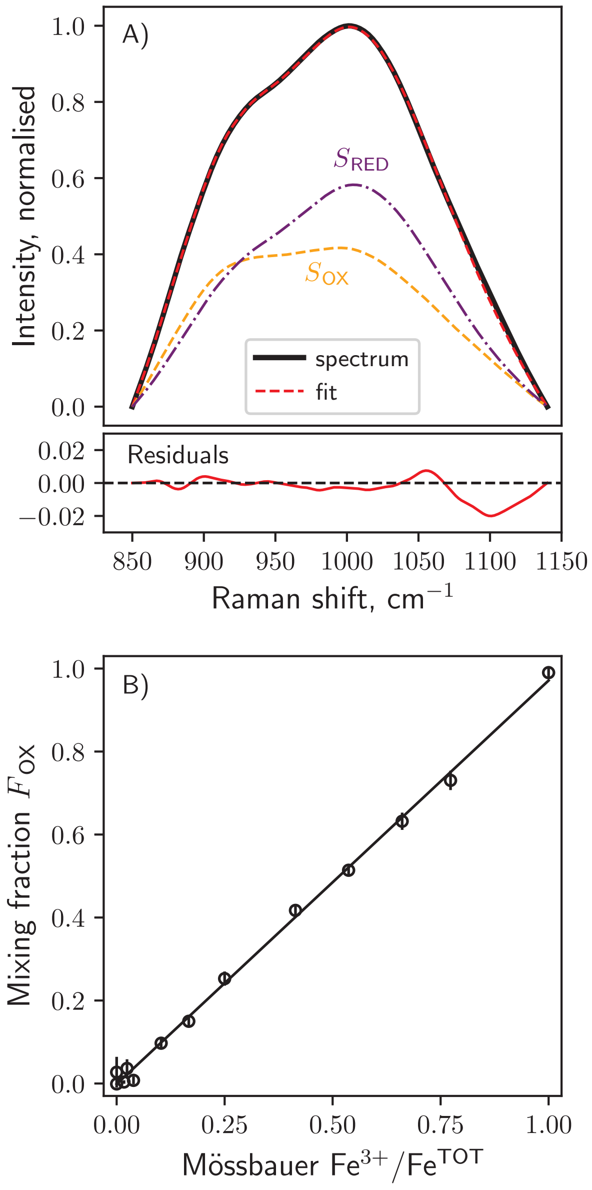A)
Intensity, normalised
1.0
0.8
0.6
0.4
0.2
0.0
S_{RED}
S_{OX}
spectrum
fit
Residuals
0.02
0.00
−0.02
850
900
950
1000
1050
1100
1150
Raman shift, cm^{-1}
B)
Mixing fraction F_{OX}
1.0
0.8
0.6
0.4
0.2
0.0
0.00
0.25
0.50
0.75
1.00
Mössbauer Fe^{3+}/Fe$^{\mathrm{TOT}}$

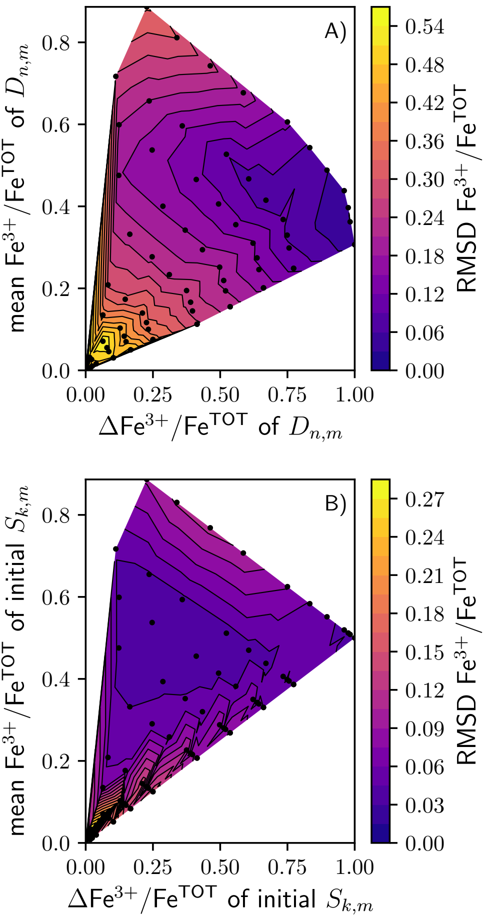
A)
mean Fe^{3+}/Fe$^{\mathrm{TOT}}$ of $D_{n,m}$
0.0
0.2
0.4
0.6
0.8
0.00
0.25
0.50
0.75
1.00
ΔFe^{3+}/Fe$^{\mathrm{TOT}}$ of $D_{n,m}$
RMSD Fe^{3+}/Fe$^{\mathrm{TOT}}$
0.00
0.06
0.12
0.18
0.24
0.30
0.36
0.42
0.48
0.54
B)
mean Fe^{3+}/Fe$^{\mathrm{TOT}}$ of initial $S_{k,m}$
0.0
0.2
0.4
0.6
0.8
0.00
0.25
0.50
0.75
1.00
ΔFe^{3+}/Fe$^{\mathrm{TOT}}$ of initial $S_{k,m}$
RMSD Fe^{3+}/Fe$^{\mathrm{TOT}}$
0.00
0.03
0.06
0.09
0.12
0.15
0.18
0.21
0.24
0.27

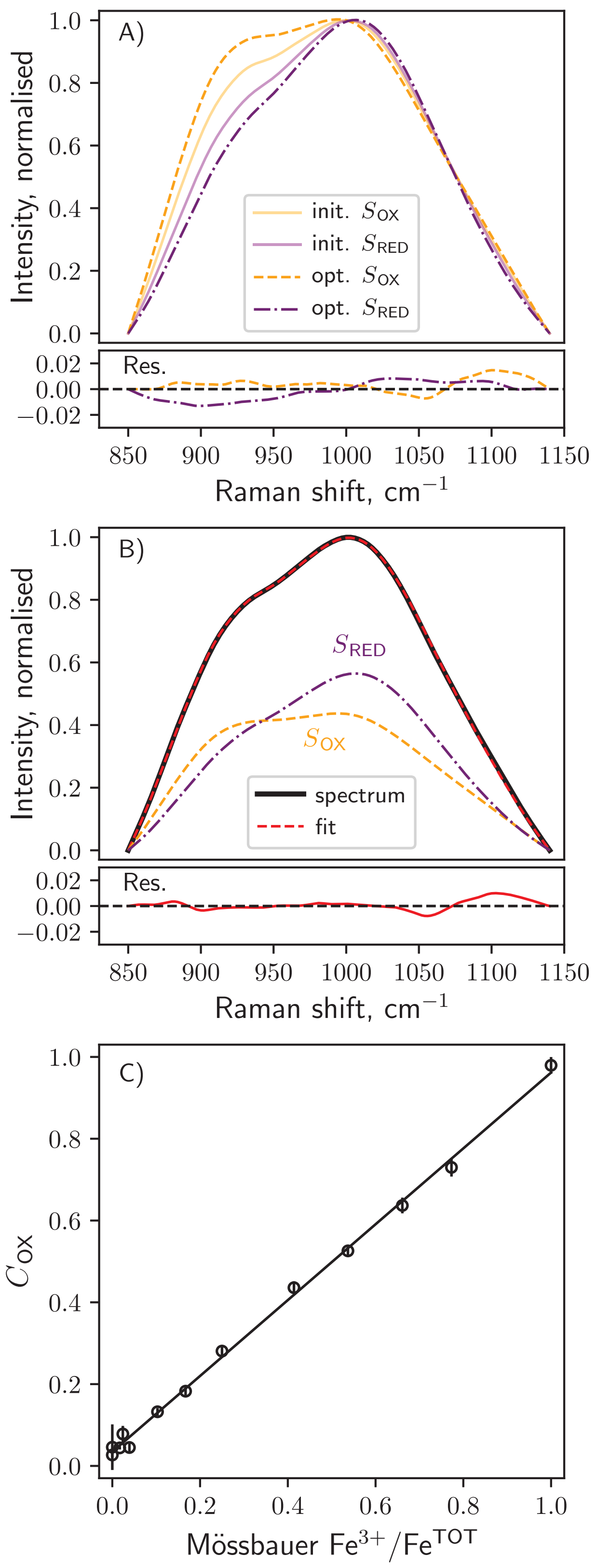
A)
Intensity, normalised
1.0
0.8
0.6
0.4
0.2
0.0
init. S_{OX}
init. S_{RED}
opt. S_{OX}
opt. S_{RED}
Res.
0.02
0.00
−0.02
850
900
950
1000
1050
1100
1150
Raman shift, cm^{-1}
B)
Intensity, normalised
1.0
0.8
0.6
0.4
0.2
0.0
S_{RED}
S_{OX}
spectrum
fit
Res.
0.02
0.00
−0.02
850
900
950
1000
1050
1100
1150
Raman shift, cm^{-1}
C)
C_{OX}
1.0
0.8
0.6
0.4
0.2
0.0
0.0
0.2
0.4
0.6
0.8
1.0
Mössbauer Fe^{3+}/Fe$^{\mathrm{TOT}}$

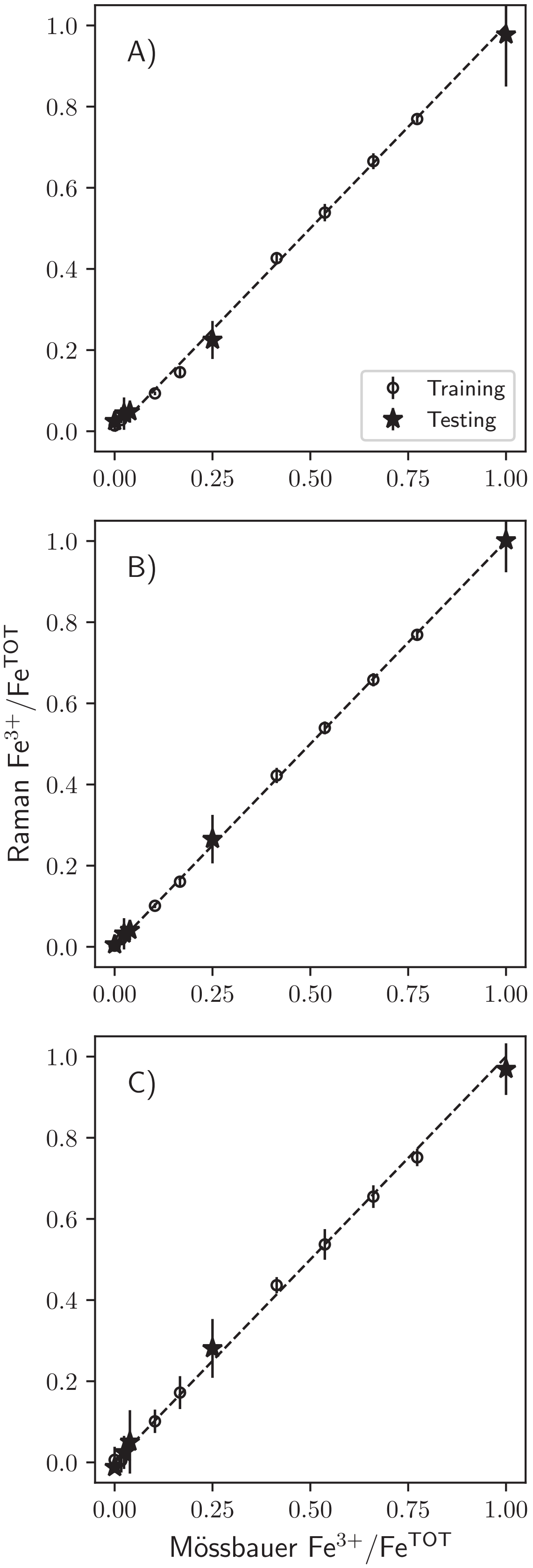
A)
B)
C)
Training
Testing
1.0
0.8
0.6
0.4
0.2
0.0
0.00
0.25
0.50
0.75
1.00
Raman Fe^{3+}/Fe^{TOT}
Mössbauer Fe^{3+}/Fe^{TOT}

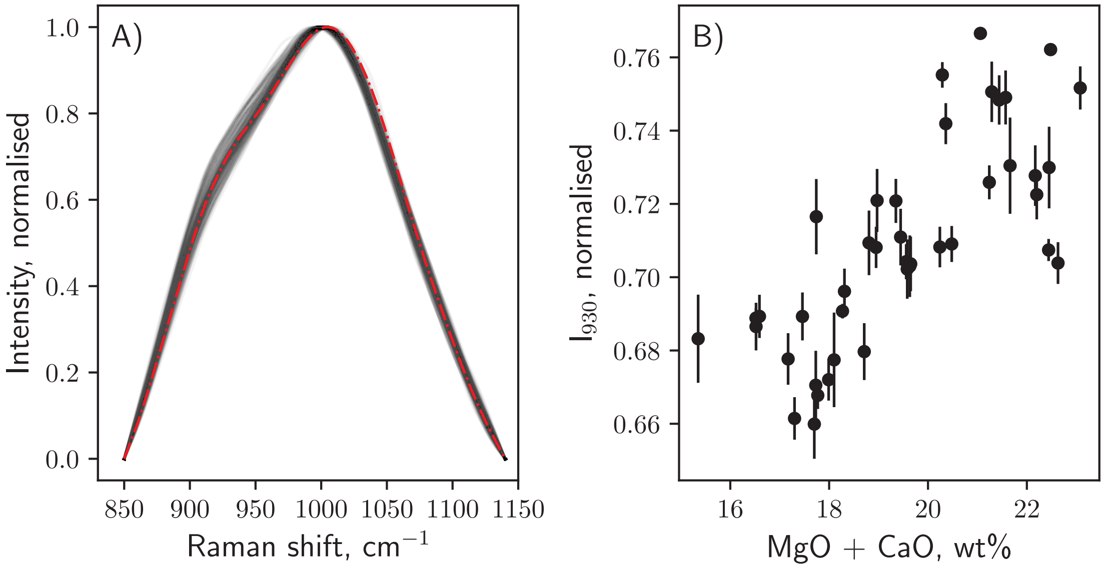
A)
Intensity, normalised
1.0
0.8
0.6
0.4
0.2
0.0
850
900
950
1000
1050
1100
1150
Raman shift, cm^{-1}
B)
I$_{930}$, normalised
0.76
0.74
0.72
0.70
0.68
0.66
16
18
20
22
MgO + CaO, wt%

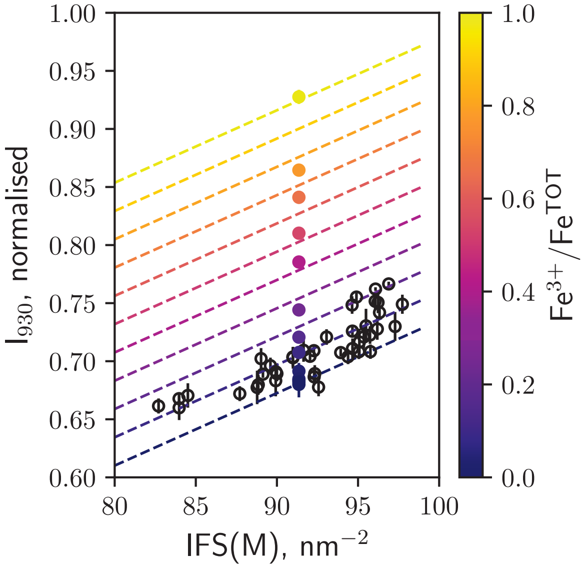
1.00
0.95
0.90
0.85
0.80
0.75
0.70
0.65
0.60
I_{930}, normalised
80
85
90
95
100
IFS(M), nm^{-2}
1.0
0.8
0.6
0.4
0.2
0.0
Fe^{3+}/Fe^{TOT}

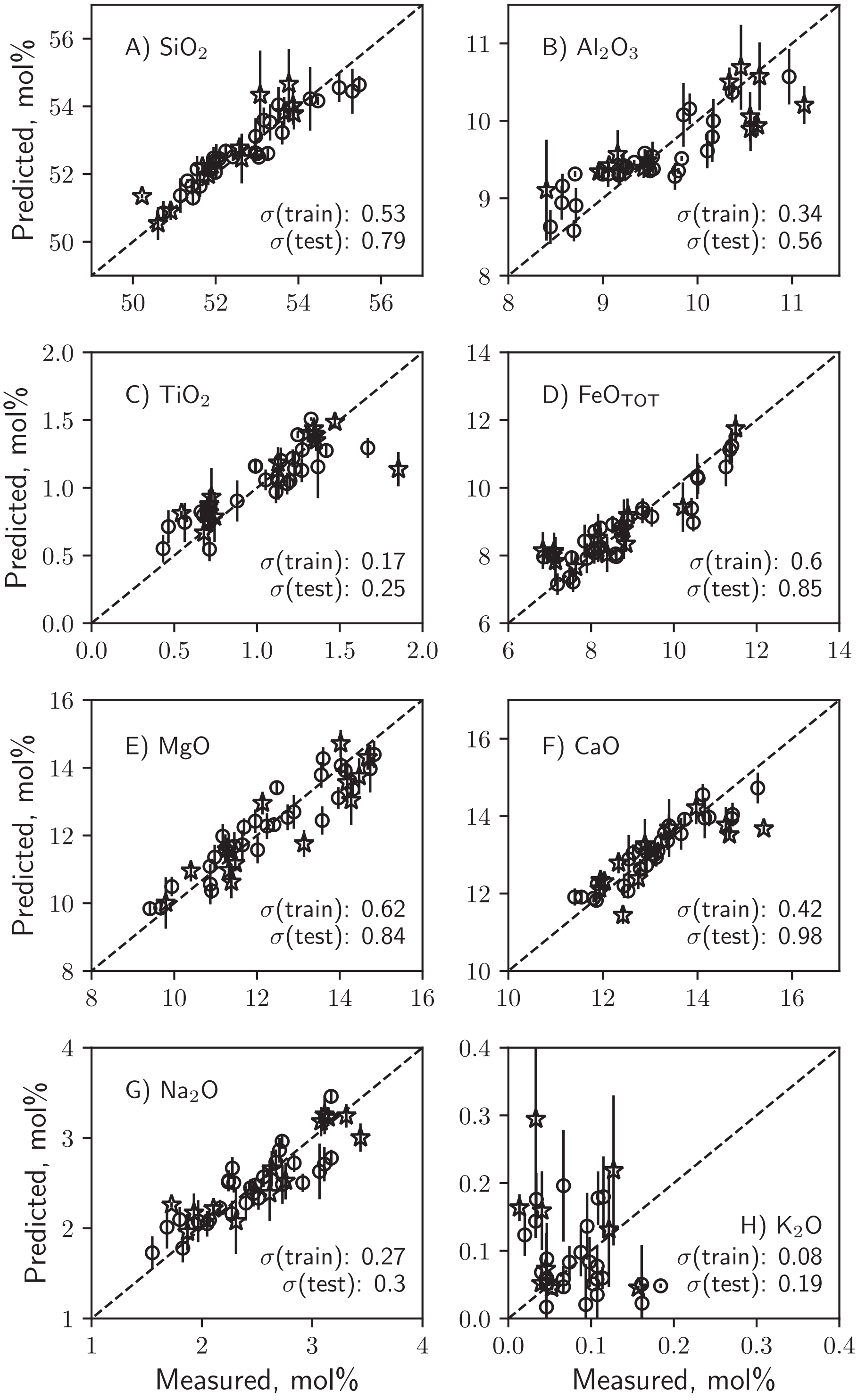
A) SiO_2
σ(train): 0.53
σ(test): 0.79
B) Al_2O_3
σ(train): 0.34
σ(test): 0.56
C) TiO_2
σ(train): 0.17
σ(test): 0.25
D) FeO_{TOT}
σ(train): 0.6
σ(test): 0.85
E) MgO
σ(train): 0.62
σ(test): 0.84
F) CaO
σ(train): 0.42
σ(test): 0.98
G) Na_2O
σ(train): 0.27
σ(test): 0.3
H) K_2O
σ(train): 0.08
σ(test): 0.19
Predicted, mol%
Measured, mol%
50
52
54
56
8
9
10
11
0.0
0.5
1.0
1.5
2.0
6
8
10
12
14
16
1
2
3
4
0.1
0.2
0.3
0.4